Scalable Binder-Free Supersonic Cold Spraying of Nanotextured Cupric Oxide (CuO) Films as Efficient Photocathodes

(Article begins on next page)

07 January 2023

Scalable Binder-Free Supersonic Cold Spraying of Nanotextured Cupric Oxide (CuO) Films as Efficient Photocathodes

Jong Gun Lee,[†] Do-Yeon Kim,[†] Jong-Hyuk Lee,[†] Min-woo Kim,[†] Seongpil An,[†] Hong Seok Jo,[†] Carlo Nervi,[‡] Salem S. Al-Deyab,[§] Mark T. Swihart,[ǁ] and Sam S. Yoon*,[†]

[†]School of Mechanical Engineering, Korea University, Seoul 136-713, Republic of Korea
[‡]Department of Chemistry, University of Torino, Via P. Giuria 7, 10125, Torino, Italy, and Consorzio Interuniversitario Reattivita ́
Chimica e Catalisi, Bari.
[§]Petrochemical Research Chair, Department of Chemistry, King Saud University, Riyadh 11451, Saudi Arabia
[ǁ]Department of Chemical & Biological Engineering, University at Buffalo, The State University of New York, Buffalo, New York
14260-4200, United States

Abstract

We demonstrate production of nanotextured ptype cupric oxide (CuO) films via a low-cost scalable supersonic cold spray method in open air conditions. Simply sweeping the spray nozzle across a substrate produced a largescale CuO film. When used as hydrogen evolution photocathodes, these films produced photocurrent densities (PCD) of up to 3.1 mA/cm^2 under AM1.5 illumination, without the use of a cocatalyst or any additional heterojunction layers. Cu$_2$O particles were supersonically sprayed onto an indium tin oxide (ITO) coated soda lime glass (SLG) substrate, without any solvent or binder. Annealing in air converted the Cu$_2$O films to CuO, with a corresponding decrease in the bandgap and increase in the fraction of the solar spectrum absorbed. Annealing at 600 °C maximized the PCD. Increasing the supersonic gas velocity from ~450 to ~700 m/s produced denser films with greater surface roughness, in turn producing higher PCD. The nanoscale texture of the films, which resembles the skin of a dinosaur, enhanced their performance, leading to one of the highest PCD values in the literature. We characterized the films by X-ray diffraction, Raman spectroscopy, X-ray photoelectron spectroscopy, atomic force microscopy, scanning electron microscopy, and transmission electron microscopy to elucidate the origins of their outstanding performance. This supersonic cold spraying deposition has the potential to be used on a commercial scale for low cost mass production.
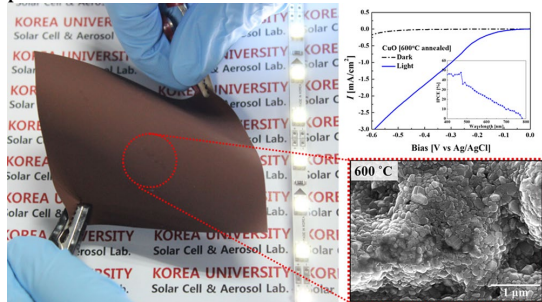
Keywords: supersonic cold spray, cupric oxide (CuO), cuprous oxide (Cu$_2$O), water splitting, nanotextured surface

1 INTRODUCTION

Copper oxide has been used in numerous applications including solar water splitting,[1–24] photovoltaics,[23,25–33] gas sensing,[34] heterogeneous catalysis,[7,16,35–37] and lithium ion batteries.[38–40] Copper oxide is nontoxic, abundant, inexpensive, and, unlike other metal oxides used in photoelctrochemical (PEC) water splitting (i.e., TiO$_2$, ZnO, Fe$_2$O$_3$, and WO$_3$), it is an efficient light absorber in the visible region of the spectrum. Copper oxide is also a relatively good electrical conductor, which facilitates extraction of photogenerated charge carriers.[7] However, the limited stability of Cu$_2$O under PEC water splitting conditions is still an issue. Cu$_2$O can be reduced to

metallic copper by photogenerated electrons, i.e., $Cu_2O + H_2O + 2e^- \rightarrow 2Cu + 2OH^-$.[15] Cupric oxide (CuO) has a bandgap in the range of $0.7-1.6$ eV,[41] while Cu_2O has a bandgap in the range of $2.0-2.2$ eV.[19] Compared to TiO_2 or Fe_2O_3 (E_g = 3.0 and 2.3 eV, respectively), both CuO and Cu_2O have a lower bandgap, which enables them to absorb nearly half of the solar spectrum (including visible light), while TiO_2 and Fe_2O_3 can capture less than 10 and 25% of the solar spectrum (mostly ultraviolet light), respectively.[10] From this perspective, CuO is superior to Cu_2O because of its lower bandgap, in spite of other issues, such as recombination and its small redox potential. Another advantage of CuO is its large absorbance coefficient, which provides equivalent light absorption by a thinner film, increasing potential flexibility of the film.[9] The large negative conduction band values of CuO and Cu_2O (i.e., $-$ 0.2 V and -0.7 V, respectively) allow them to be used as efficient hydrogen-generating electrodes. CuO and Cu_2O have theoretical maximum photocurrent densities (PCD) of 35 and 14.7 mA/cm2, respectively, under 1.5 AM irradiation.[15] To date, the highest PCD achieved is that reported by the Gratzel group[7] with a value of 7 mA/cm2 using electrodeposited Cu_2O. They also reported a breakthrough in improving the stability of a copper oxide film by introducing multiple protective layers using ZnO and TiO_2 together with platinum cocatalysts. However, the coating process requires at least five layers each of ZnO and TiO_2, which increases the manufacturing cost, not to mention the cost of materials such as platinum or palladium.[14] Cu_2O has a moderately high bandgap of $2.0-2.2$ eV, which is larger than the required minimum water oxidation potential of 1.23 eV; however, the Cu_2O bandgap remains in the visible light range. For these reasons, much research has been devoted to investigating Cu_2O as a photocathode, especially since the work of Paracchino et al.[7]
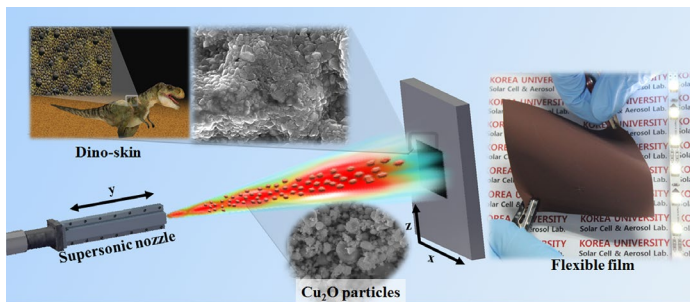

Figure 1. Schematic of cold spray deposition (middle inset image is the SEM image of CuO after air annealing).

Given the advantages of Cu_2O, there has been comparatively less research into CuO as a photocathode material. However, CuO is more stable than Cu_2O[13,19] and thus is often used as a protective layer over Cu_2O. Simple air annealing transforms Cu_2O into CuO. Furthermore, CuO has the advantage of a smaller bandgap, allowing it to absorb more of the solar spectrum, and producing its very high theoretical PCD of 35 mA/cm2. CuO films have been fabricated using sputtering,[23,24] spin coating,[5,14,42] direct anodization,[22] sol$-$gel spin-coating,[15] physical vapor deposition,[19] and hybrid microwave annealing[17] techniques. Most of these studies yielded PCD values below 2.0 mA/cm2. Notable exceptions are the work of Masudy-Panah et al. and Jang et al., who produced PCD values of 2.5 and 4.4 mA/cm2, respectively. Masudy-Panah et al.[23] showed that their enhanced PCD could be attributed to the increased effective surface area upon increasing the sputtering power used in CuO deposition. Jang et al.[17] also increased the surface area using hybrid microwave annealing process which produced a unique hierarchical leaf-shaped morphology. On the basis of this observation, we infer that increasing the surface area is a key factor in maximizing the PCD of the CuO film.

Here, we have increased the surface area of our CuO films by increasing the impact velocity of Cu_2O particles deposited by supersonic spray deposition. Supersonic spraying facilitates in situ nanotexturing of film surfaces via the high-speed impact. Nanotextured surfaces are obtained by the deposition of irregular nanoparticles that are pulverized upon impact. Subsequent annealing converts the films to CuO and improves film crystallinity. The supersonic cold spray deposition was conducted in open air conditions, and simply sweeping the nozzle across a substrate produced a large-scale CuO film. Therefore, this deposition method has the potential to be used on a commercial scale for low cost mass production. The films produced here were rigorously characterized by X-ray diffraction (XRD), Raman spectroscopy, X-ray photoelectron spectroscopy (XPS), atomic force microscopy (AFM), scanning electron microscopy (SEM), and transmission electron microscopy (TEM). The effect of the supersonic impact velocity on the PCD was also investigated. The mechanism of the improved PCD was explained by the change in bandgap and surface roughness as a function of the impact velocity. The nanotextured surface morphology interestingly resembles the skin of a dinosaur.

2 EXPERIMENTAL SECTION

2.1. Supersonic Cold Spraying. Figure 1 depicts the supersonic cold spraying method used here. Cu_2O particles were sprayed at a supersonic velocity via a converging-diverging nozzle. Upon impact, they were pulverized, and their fragments adhered to a flexible substrate to produce a thin film. The Cu_2O film was sufficiently conductive to turn on an LED light in a wired electrical circuit, as demonstrated in the right-hand inset of Figure 1. Films of $1-3$ μm thickness were grown by sweeping the spray nozzle across the substrate 15 to 25 times at a scan speed of 10 mm/s. The pulverized fragments underwent in situ sintering upon impact, as their kinetic energy was converted to thermal energy. The supersonic gas velocity was determined by the operating pressure and temperature of the air, which were in the range of $2 \leq P_0 \leq 4$ bar and $250 \leq T_0 \leq 450$ °C, respectively (see Table 1), yielding an isentropic air velocity of $553-829$ m/s. As the ball-milled particles used here are small, their Stokes number is also small (Stk $\approx 10^{-4}$), and the velocity of the entrained nanoparticles nears that of the air.[43,44] More details on cold spraying deposition are provided in our previous work.[45-47]

Table 1. Operating Conditions for the Supersonic Cold Spraying System

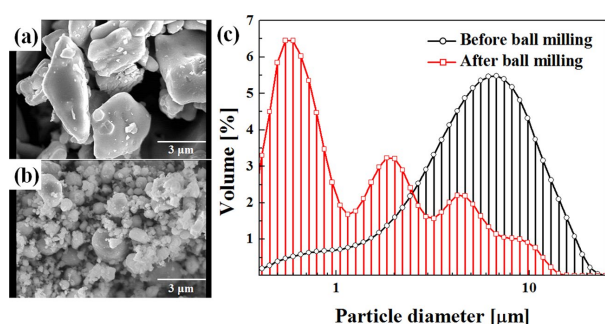| Conditions	
Pressure [bar]	$2-4$
gas preheating temperature [°C]	$250-450$
traverse speed [mm/s]	10
nozzle-to-substrate distance [mm]	50

Figure 2. SEM images of Cu_2O particles (a) before and (b) after 4 days of ball milling; and (c) particle size distribution of Cu_2O particles from a laser-diffraction particle size analyzer before and after ball milling.

2.2. Cuprous Oxide (Cu_2O) Precursor. As shown in Figure 2a and b, Cu_2O particles with an average size of 6.5 μm were ball-milled into smaller particles, which were then fed into the cold spray coating system, as depicted in Figure 1. As shown in Figure 2c, the particle size was significantly reduced after 4 days of ball milling. The milled material had a broad trimodal size distribution. A substantial fraction of the particles was below 1 μm in diameter, which is desirable for the cold spraying process. If a particle is too large, then the particle response time is also large, and the particle is not accelerated to the gas velocity before impact. If the particle size is too small, then the particles do not attain sufficient momentum to be fragmented upon impact. On the basis of our prior experience, an average particle size of 1 ± 0.5 μm is most effective.[45]

2.3. Characterization of the Photoelectrodes. The distribution of particle sizes was analyzed using a laser-diffraction particle size analyzer (LS 13 320, Beckman Coulter, U.S.A.), as well as by direct scanning electron microscopy (SEM, S-5000, Hitachi, JAPAN) imaging. Crystallinity and crystal phase were assessed using powder X-ray diffraction (XRD, SmartLab, Rigaku, JAPAN) across a range of $10° < 2\theta < 80°$ and by Raman spectroscopy, using a confocal Raman spectrometer (NRS-3100) with a 532 nm laser excitation source. The chemical composition of the surface of the films was studied by X-ray photoelectron spectroscopy (XPS, Theta probe base system, Thermo Fisher Scientific Co.). The morphology of the CuO thin films was studied using SEM (S-5000, Hitachi, JAPAN) at 10 kV and transmission electron microscopy (TEM, JEM 2100F, JAPAN). The TEM specimen was prepared using focused ion beam milling (FIB, LYRA3 XMH, Tescan). Atomic force microscopy (AFM, XE-100, Park Systems, KOREA) was used to measure the surface roughness of the films.

2.4. Photoelectrochemical (PEC) Measurements. A single cell with three electrodes was used for PEC measurements. Each of the CuO films was used as the working electrode, while an Ag/AgCl rod and platinum wire were used as the pseudo reference and counter electrodes, respectively. These three electrodes were positioned with interelectrode distances of 10 mm, and their positions were fixed in order to acquire consistent data and minimize transport limitations in the electrolyte. The sample area exposed to the illuminating light was 0.25 cm^2. A 1 M KOH (pH = 14) solution was used as the electrolyte. Nitrogen gas was purged through the electrolyte solution to remove any dissolved oxygen before the measurements. Artificial sunlight from a xenon arc lamp (Newport, Oriel Instruments, U.S.A.) equipped with an AM 1.5 filter was used as a light source with an intensity of 100 mW/cm^2. All photocurrent data were recorded using a potentiostat (VersaSTAT-3, Princeton Applied Research, U.S.A.) with a scan rate of 10 mV/s and an applied voltage ranging from 0.5 to -0.6 V relative to Ag/AgCl.
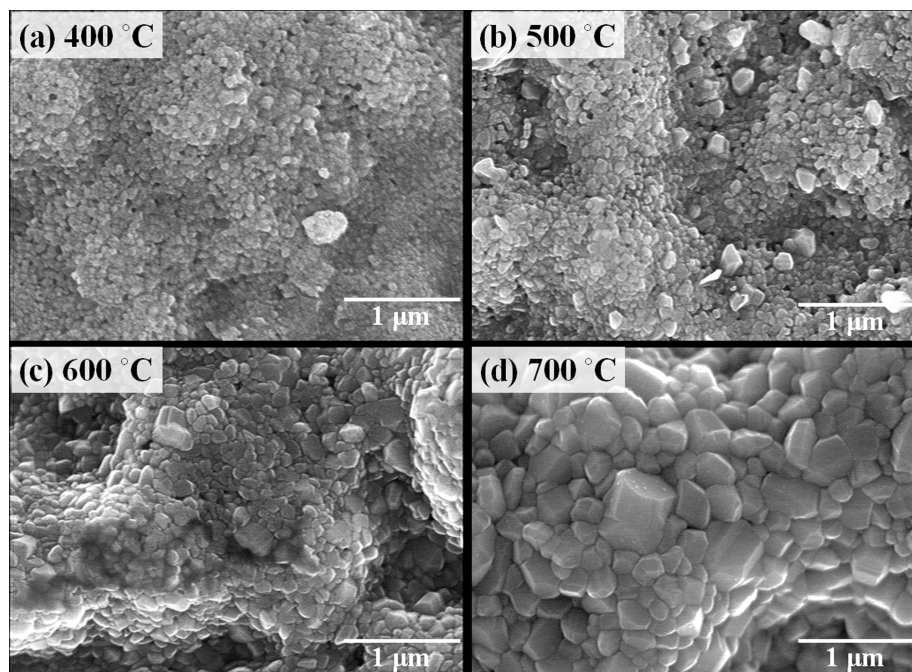
3 RESUTS and DISCUSSION

Figure 3. Effect of annealing temperature on the CuO surface morphology, (a) 400 °C, (b) 500 °C, (c) 600 °C, and (d) 700 °C.

3.1. Effects of Annealing. Figure 3 shows the surface morphology of films annealed at 400 °C, 500 °C, 600 °C, and 700 °C. All the films exhibited surface curvature (peaks and valleys at a length scale much larger than the individual particles). This irregular surface, which forms spontaneously upon fragmentation of the impacting particles, resembles the self-induced honeycomb structure previously reported for aerosol-deposited films.[48] This type of spontaneous nanostructuring enhances the accessible surface area of the film. Figure 3 also shows the increase in crystal size with increasing annealing temperature, consistent with sharpening of XRD peaks in Figure 4. The small pulverized nanoparticles are of uniform crystal size, as shown in Figure 3a and are substantially smaller than the precursor Cu_2O particles. Upon increasing the annealing temperature, these small crystals coalesced and grew, as is evident from Figure 3b. At 600 °C, the growth of the crystals on the irregular surface of the film resembles the rough skin of a dinosaur. Crystal growth can improve the PEC performance of the CuO by improving the transport of charge carriers and reducing the total number of recombination centers. However, excessive growth may hinder water splitting performance by reducing the effective surface area, which is generally inversely proportional to the crystal size.

Figure 4 shows XRD patterns from the Cu_2O nanoparticles, the as-deposited film, and films annealed in air at 400 °C, 500 °C, 600 °C, and 700 °C for 30 min; all films were fabricated under the operating conditions of P_0 = 4 bar, T_0 = 450 °C. Diffraction peaks at 2θ values of 29.6°, 36.4°, 42.4°, and 61.4° corresponds to the (110), (111), (200), and (220) planes of Cu_2O, respectively. After annealing, the Cu_2O diffraction peaks are replaced by those of CuO, with two prominent peaks at 35.66° and 38.85°, corresponding to lattice spacings (dspacings) of 0.25 and 0.23 nm, respectively. These peaks arise from diffraction by the (−111)/(002) and (111)/(200) planes of CuO (JCPDS card no. 801917). Annealing at temperatures above 400 °C did not result in any further phase change. In air, the conversion of Cu_2O to CuO occurs below 400 °C.[19,49] Valladares et al.[49] and Basnet el al.[19] reported that the transformation of Cu_2O into CuO started at 150−200 °C. Although the peak positions do not change with increasing annealing temperature above 400 °C, the peaks do become sharper at higher annealing temperatures, indicating improved crystallinity and increased crystallite size. The crystal size was determined from the Debye −Scherrer formula, $D = 0.9\lambda/(\beta \cos \theta)$, where D is the crystal size, λ is the X-ray wavelength, β is the full width at half-maximum (fwhm) of the diffraction peak, and θ is the diffraction angle. The estimated crystal size increased from 32.1 nm to 34.7, 40.7, and 43.5 nm as the annealing temperature increased from 400 to 700 °C. It should be noted that the diffraction peak at 2θ = 31°arises from the ITO coating on the substrate. At higher temperatures of 600 °C and 700 °C, the ITO peak is not visible because it is smaller relative to the CuO peaks, which become stronger with increasing annealing temperature.
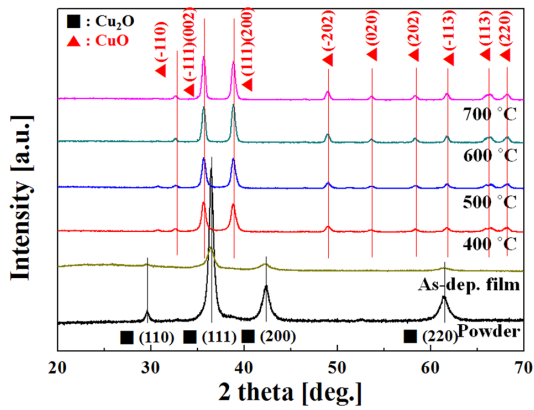
Figure 4. XRD pattern of Cu_2O powder, as-deposited film, and films annealed at 400 °C, 500 °C, 600 °C, and 700 °C.
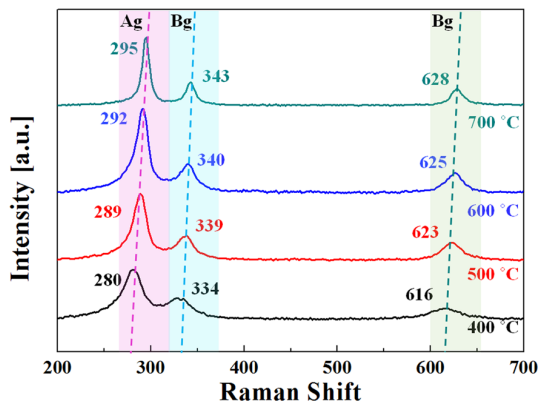

Figure 5. Raman spectra of CuO films annealed at 400 °C, 500 °C, 600 °C, and 700 °C.

We also employed Raman spectroscopy, with 532 nm excitation, scanning from $200-700$ cm^{-1} to characterize the CuO films annealed in air at 400 °C, 500 °C, 600 °C, and 700 °C. CuO is included in the C_{2h}^6 space group with binary molecules for a given unit primitive cell. CuO is also included in the normal modes of the center zone, namely, Γ_{RA} = 4Au + 5Bu + Ag + 2Bg, which comprises 3 acoustic modes of (Au + 2Bu), 6 infrared active modes of (3Au + 3Bu), and 3 Raman active modes of (Ag + 2Bg).[50] Raman spectra of the CuO films deposited on an indium tin oxide (ITO)-coated soda lime glass (SLG) substrate (Figure 5) show three peaks corresponding to the three Raman active optical phonons at 280, 334, and 616 cm^{-1}. The peak at 280 cm^{-1} is due to the Ag mode and the peaks at 334 and 616 cm^{-1} are due to the Bg modes.[51] Raman peaks of the CuO film became sharper and stronger and shifted to higher wavenumbers with increasing annealing temperature. For example, the peak at 280 cm^{-1} shifted to 289, 292, and 295 cm^{-1}, while the fwhm of the peaks decreased from 19.93 cm^{-1} to 15.66, 14.24, and 8.54 cm^{-1} as the annealing temperature increased from 400 °C to 700 °C. The peak positions after 700 °C annealing are very close to those reported for bulk, singlecrystalline CuO, which are 297, 344, and 629 cm^{-1}.[52]
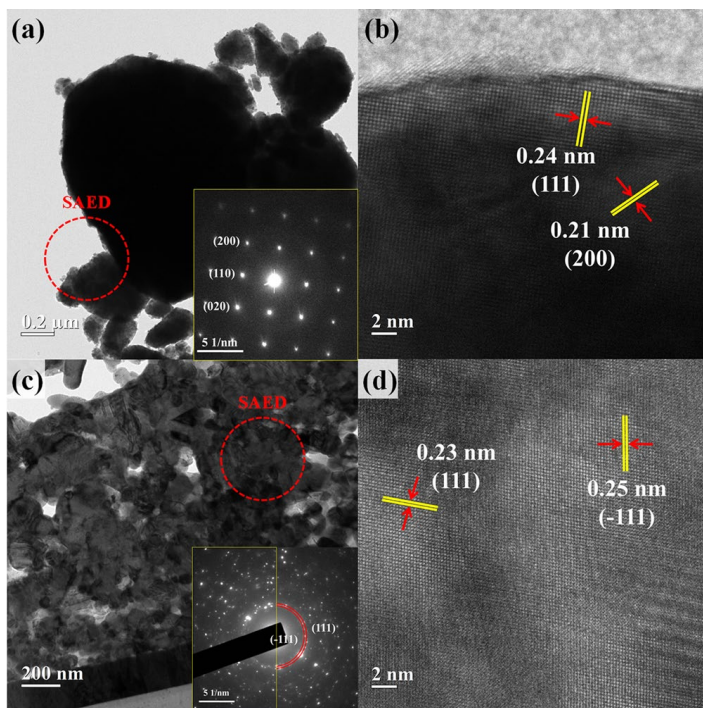
Figure 6. (a) Low magnification TEM image, Inset: Selected area electron diffraction (SAED) pattern, (b) High-resolution TEM image (HRTEM) of Cu_2O powder, (c) Low magnification TEM image Inset: SAED pattern, and (d) HRTEM image of CuO film.

The morphology and crystallographic structure of the Cu_2O particles and CuO film were also analyzed by TEM. Figure 6a and b displays TEM images of the Cu_2O particles. Figure 6a shows the low magnification TEM image and the selected-area electron diffraction (SAED) pattern (as an inset). The SAED pattern from the region marked by the red circle corresponds to the expected pattern for diffraction from Cu_2O along the [002] zone axis, with spots due to diffraction by the (200), (110), and (020) planes. The high-resolution TEM (HRTEM) image shown in Figure 6b shows clear lattice fringes at spacings of 0.24 and 0.21 nm, which were assigned to the (111) and (200) plane of monoclinic Cu_2O, respectively.[53,54] Figure 6c displays a low-magnification TEM image of the CuO film, which was prepared by a focused ion beam (FIB) technique. The SAED pattern (inset) shows two diffraction rings on the image corresponding to (111) and (−111) planes, respectively, along with numerous higher-order diffraction spots. The complexity of the pattern reflects the polycrystalline nature of the film. The detailed microstructure of the CuO film was revealed by HRTEM, as shown in Figure 6d. The lattice fringes between two planes of an isolated particle were calculated to be 0.23 and 0.25 nm, which were assigned to the (111) and (−111) planes of monoclinic CuO, respectively.[42,55,56] The HRTEM and SAED analyses confirmed the phase transformation into CuO.
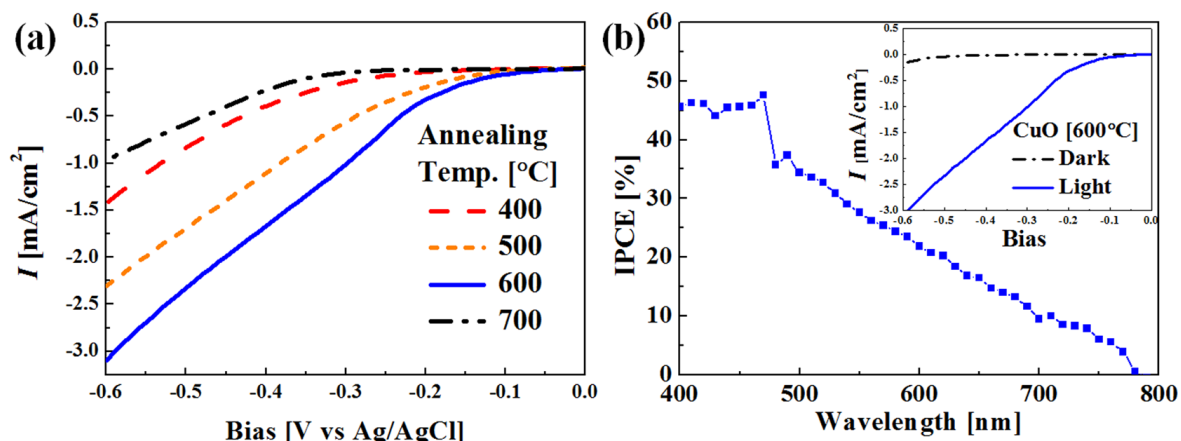

Figure 7. (a) Effect of annealing temperature on the current−potential curves of CuO photocathodes measured at 1 sun (1.5 AM filter) illumination in 1 M KOH (pH = 14). (b) IPCE of CuO photocathode. Inset: Dark and light current−potential curves for 600 °C.

The performance of the cold sprayed CuO films as photocathodes for PEC water-splitting was studied by measuring PCD vs voltage with respect to the Ag/AgCl reference electrode. The results for CuO films annealed at temperatures of 400 °C, 500 °C, 600 °C, and 700 °C are shown in Figure 7a. All of these films were deposited using a fixed air pressure and temperature of P_0 = 4 bar and T_0 = 450 °C. All measurements were performed under AM 1.5 (100 mW/cm^2) illumination and using 1 M KOH (pH = 14) as the electrolyte. A platinum wire was the counter electrode and CuO was the working photocathode. Current−potential (I−V) curves were measured with (light) and without (dark) illumination. The dark current densities of the films were very low, typically a few μA, as shown in the inset in Figure 7b. The low dark current demonstrates that the PCD values under illumination are not due to simple corrosion or other nonphotoinitiated processes, although the small current near −0.6 V may reflect the onset of corrosion reactions. Under illumination, photogenerated electron−hole pairs form in the valence band of the CuO film. After separation, the electrons travel to the conduction band of CuO and reduce water molecules at the solid−liquid interface, generating $H_2(g)$ and $OH^-(aq)$. The OH^- is oxidized at the counterelectrode to produce O_2 and water. Paracchino et al.[7] used atomic layer deposition (ALD) to deposit TiO_2 and ZnO layers, which produced a PCD value of −7.6 mA/cm^2 at 0.25 V while promoting the electron transport or mobility. In addition, these TiO_2 and ZnO layers protected the Cu_2O (cuprous) layer from corrosion by avoiding the direct contact between Cu_2O and electrolyte. Without the ALD layers, they achieved a PCD value of −2.4 mA/cm^2, which is less than our best case of −3.1 mA/cm^2 shown in Figure 7a. As shown in Figure 7a, the onset potential for each film was in the range of −0.1 V to −0.25 V. From 400 °C to 500 °C to 600 °C, the onset potential moved to the right, producing higher PCD. At 600 °C, PEC performance reached a maximum of −3.1 mA/cm^2 at −0.6 V. Annealing at 700 °C dramatically diminished the PCD. The maximum PCD values, at −0.6 V, obtained for films annealed at 400 °C, 500 °C, 600 °C, and 700 °C were −1.4, − 2.3, − 3.1, and −1.0 mA/cm^2, respectively. Note that −0.6 V is the potential limit at which the film corrosion begins, yielding a nonzero dark current value. As mentioned earlier, there is a trade-off between crystal size and effective surface area. Smaller crystal size can provide a larger accessible surface area for reaction. However, if the crystal size is too small, then charge carrier transport will be inhibited. Improving crystallinity reduces the concentration of defect sites at which photogenerated charge carriers can recombine and improves carrier mobility and charge separation.[57,58] Thus, there is crystal size that optimizes the trade-off between improved charge carrier transport and reduced reactive surface area. The XRD pattern from Figure 4 shows the crystallinity of the 600 °C film is nearly equivalent to that of the 700 °C film. However, as shown in the SEM of Figure 3, the 600 °C film maintains a much smaller particle or crystallite size at the film surface, providing a much larger accessible surface area and number of sites for PEC. In addition, the onset potential is also significantly influenced by the postannealing temperature. The onset potential for the film postannealed at 600 °C is about −0.1 V which shifted significantly to −0.25 V after 700 °C annealing. Comparing the SEM images of films annealed at 600 and 700 °C reveals that the film annealed at 700 °C not only has larger average crystal size, and therefore smaller surface area, but is also significantly more faceted. Reconstruction of the film to expose only low energy facets may reduce its catalytic activity, i.e., the most reactive sites are likely to be at edges, vertices, and high-energy facets, many of which have been removed by annealing at 700 °C. In addition, higher annealing temperature increases the possibility of diffusion of impurities from the ITO-coated SLG into the CuO film, introducing defect sites that can serve as recombination centers for charge carriers. Hence, multiple factors may contribute to the decreased performance of the film annealed at 700 °C.

Figure 7b shows the incident photon-to-current efficiency (IPCE) data of the 600 °C film acquired at −0.6 V vs Ag/AgCl for a wavelength range of 400−800 nm. IPCE is an indicator of light harvesting capability in the tested wavelength range. The onset of photocurrent near 800 nm corresponds to an effective band gap of about 1.5 eV, which is near the optimum bandgap for light harvesting. The CuO film showed a maximum IPCE of 47.6% at λ = 470 nm, well into the visible portion of the solar spectrum. This IPCE value of 47.6% is quite high in comparison with previous studies: Hsu et al.[59] fabricated CuO nanowires on a copper foil via thermally transferring and reported an IPCE value of 15%. Wang et al.[18] used a wet chemical method and a hydrothermal process to fabricate ZnO/CuO bilayers and reported an IPCE value of 10%.

Table 2. Cold Spray Operation Details

	case 1	case 2	case 3	case 4	case 5	case 6	case 7	case 8	case 9
operating pressure (bar)	2	2	2	3	3	3	4	4	4
operating temperature (°C)	250	350	450	250	350	450	250	350	450
gas velocity (m/s)	553	585	615	677	716	753	746	789	829
Stokes no. $\times 10^{-4}$ (Stk)	3.79	4.13	4.43	4.64	5.05	5.43	5.11	5.56	5.98
sheet resistance (Ω/sq)	41.2	43.4	44.5	51.6	44.9	51.5	53.7	57.5	72.7
roughness (μm)	0.10	0.15	0.17	0.10	0.14	0.17	0.10	0.15	0.18
photocurrent density (mA/cm²)	−0.5	−0.7	−1.8	−0.7	−1.2	−2.3	−1.5	−1.9	−3.1
crystal size (nm)	37.9	37.5	37.9	37.0	38.8	39.7	37.9	38.8	40.7

[a]Note that velocity from Case 7 is lower than that from Case 6.

3.2. Effect of Impact Velocity. Successful cold spray deposition depends on achieving appropriate gas velocity, which determines the kinetic energy of the impacting particles. Here, we varied the air pressure and temperature of the gas supplied to the nozzle to change the particle impact velocity and studied the effects on the PEC performance. Particles entrained into the supersonic stream quickly reach the gas stream velocity. Their ability to respond to changes in gas velocity is characterized by a Stokes number (Stk), defined as $Stk = \tau_p/\tau_g$, where $\tau_p = \rho_p D^2/(18\,\mu_g)$ is the particle response time to the surrounding supersonic stream, and $\tau_g = d/V_e$ is the characteristic time for impingement of the supersonic stream; ρ_p and D are the particle density and diameter, respectively; μ_g is the gas dynamic viscosity, and d and V_e are the nozzle exit diameter and air velocity. Isentropic gas velocity at the supersonic nozzle exit is calculated as follows:

$$V_e = \sqrt{2c_p T_o [1 - (P_e/P_0)^{(\gamma-1)/\gamma}]} \quad (1)$$

where c_p is the specific heat, and T_0 and P_0 are the carrier source temperature and pressure, respectively. The specific heat ratio of an air was $\gamma = 1.4$. The pressure at the nozzle exit is P_e. The gas velocity at the nozzle exit was multiplied by a factor of 0.8 to estimate the particle velocity of V_p (i.e., $V_p \approx 0.8V_g$), based on the calculated Stokes number.[43] Table 2 summarizes the nozzle exit velocity and Stokes number for various combina-
tions of pressure and temperature of the carrier gas. The electrical sheet resistance of the CuO film was in the range of 41–73 Ω/sq, which is relatively low compared to other oxide films such as reduced graphene oxide. This high electrical conductivity is important in supporting carrier transport across the film, which is necessary for achieving high PCD values.

There have been some reports that Cu_2O and CuO composites yield the best PEC performance.[13] This may be because the light absorption and catalytic activity of the two copper oxides complement one another, such that the best PEC performance was achieved from optimal proportions of the two copper oxides, which were adjusted by controlling the annealing temperature.[49] However, in our case, the as-deposited Cu_2O film was not capable of allowing sufficient current flow and thus no PCD was detected. This poor performance of the Cu_2O film was probably because of the poor crystallinity of the as-deposited film, as shown in Figure 3. In our case, the films were intensely densified and a surface with severe curvature was produced by increasing the impact velocity. The film densification had a favorable effect on the electron–hole transfer. The severe curvature of the films increased the effective surface area for maximal interfacial PEC
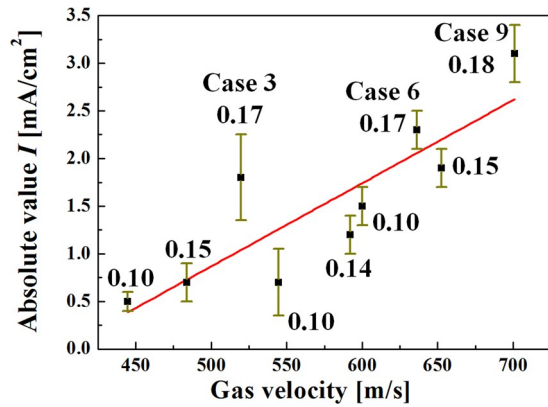activity.

Figure 8. Effect of gas velocity (operating conditions) on the current− potential curves of CuO photocathodes measured at 1 sun (1.5 AM filter) illumination in 1 M KOH (pH = 14). The numbers shown for all points are the surface roughness values in microns.

Figure S1 shows SEM images of the CuO films annealed at 600 °C for the various impact velocities summarized in Table 2. Film densification is clearly shown as voids are removed with increasing impact velocity. There is no discernible difference in the surface morphology for the P_0 = 2 bar cases (which are Cases 1, 2, and 3 in Table 2). However, Case 3 produced the best PCD (−1.8 mA/cm²) of all three cases. For the P_0 = 3 bar cases, the appearance of the "dinosaur skin" texture gradually progresses and is apparent in Case 6. While comparing the P_0 = 4 bar cases, the surface texturing appears to be similar; however, the roughness was highest for Case 9. There is a common factor in Cases 3, 6, and 9: They are the cases with the highest roughness among the compared cases. Thus, we conclude that surface roughness is the major factor dominating the PEC performance for the cold sprayed films, which we have achieved by increasing the impact velocity.

Table 3. Comparison of the PEC Performance of the Present CuO Thin Films with Literature Values

coating method	incident light [mW/cm²]	*Reactant solution [M]*	applied potential [V Ag/AgCl][f]	pH	photocurrent density [mA/cm²]	reference
sputtering	125	0.4[a]	−0.50	11	−0.24	24
spin coating	100	1.0[b]	−0.55	14	−1.20	35
spin coating	100	1.0[b]	−0.55	14	−1.20	10
direct anodization	N.A.	0.5[c]	−0.36	7.29	−0.36	22
spin-coating	100	0.1[d]	−0.60	5.84	−0.55	15
spin coating	100	0.2[e]	−0.55	9.2	−1.50	14
hybrid microwave annealing	100	1.0[d]	−0.55	6	−4.40	17
physical vapor deposition	100	0.5[d]	−0.50	6.4	−0.24	19
sputtering	100	0.1[d]	−0.55	5.84	−2.50	23
cold spraying	100	1.0[b]	−0.60	14	−3.10	present work

Figure 8 clearly shows the pattern of increasing PCD with increasing impact velocity. First, this improved photocathode performance with increasing impact velocity can be explained by the associated reduction in the bandgap (see Figure S2).

Second, the rougher surface morphology was another reason behind the higher PCD values (see the roughness data in microns for Cases 3, 6, and 9). Films with a roughness greater than R_z = 0.15 μm tended to yield higher PCD values. Roughness alone cannot be the only reason behind this trend because sometimes a smaller roughness (as in Case 7 with a roughness of 0.1 μm) produces a higher PCD value as compared to cases with higher roughness (as in Cases 2 and 5 with a roughness of 0.15 and 0.14 μm, respectively). The film densification effect also contributes to the enhancement of the electron−hole transfer with increasing impact velocity. However, there is strong evidence to show that roughness has a strong influence on the overall PEC performance.

[Table 3](#) compares the PEC performance of our CuO films against films from previous studies reported since 2010. Our supersonic cold sprayed CuO films exhibited a PCD of −3.1 mA/cm^2, which is the best of all the reported values except for the PCD reported by Jang et al.,[17] which was −4.4 mA/cm^2. The high performance of our films is remarkable considering that they are produced by a rapid, scalable, and non vacuum process. To coat the 7 × 7 cm^2 sized film using supersonic cold spraying (see the inset in [Figure 1](#)) required a spraying time of less than 30 s using one nozzle, and the process could be carried out under open atmospheric conditions. Other methods such as sputtering or PVD require a vacuum chamber, and as a result are time-consuming and not readily scalable. Spin coating is simple, but much slower, and makes inefficient use of film precursors by ejecting most of the material from the spinning surface. In conclusion, none of the previously reported PCD values compared favorably with our current value of −3.1 mA/ cm^2. Jang et al. reported a higher PCD value of −4.4 mA/cm^2 using a hybrid microwave annealing process with a silicon susceptor, which required both post thermal treatments and microwave synthesis.[17] Jang et al. showed that the leaf-like structures of the CuO film they produced provided an increased surface area and thus a larger number of interfacial activities, which is in agreement with our findings herein. Compared to the hybrid microwave annealing process, our cold spraying method is simpler and scalable and thus would be beneficial to the commercialization of the technology. A 7 × 7 cm^2 CuO film deposited on a flexible copper foil was fabricated within 30 s of spraying, demonstrating the scalability and potential use in commercial applications.[46,47,60]

CONCLUSIONS

Supersonic cold spraying was used to deposit Cu_2O nano- particles on an ITO-coated SLG substrate for the fabrication of photocathodes for use in solar water splitting. The deposited Cu_2O films were sintered at various annealing temperatures to convert them to CuO and improve their crystallinity. The optimal annealing temperature was 600 °C, which produced a moderate crystal size that optimized the trade-off between high surface area of small crystals and better charge carrier transport in larger crystals. The supersonic gas temperature and pressure were varied in the range of 250 < T_0 < 450 °C and 2 < P_0 < 4 bar, respectively. The CuO film fabricated at T_0 = 450 °C and P_0 = 4 bar yielded the best PCD of −3.1 mA/cm^2 and exhibited the highest roughness and densification due to the highest impact speed.

REFERENCES
(1) Chaudhary, Y. A Study on the Photoelectrochemical Properties of Copper Oxide Thin Films. Int. J. Hydrogen Energy 2004, 29, 131−134.
(2) Bandara, J.; Udawatta, C. P.; Rajapakse, C. S. Highly Stable CuO Incorporated TiO$_2$ Catalyst for Photo-catalytic Hydrogen Production from H$_2$O. Photochem. Photobiol. Sci. 2005, 4, 857−861.
(3) Barreca, D.; Fornasiero, P.; Gasparotto, A.; Gombac, V.; Maccato, C.; Montini, T.; Tondello, E. The Potential of Supported Cu$_2$O and CuO Nanosystems in Photocatalytic H$_2$ Production. ChemSusChem 2009, 2, 230−233.
(4) Wu, L.; Tsui, L.-k.; Swami, N.; Zangari, G. Photoelectrochemical Stability of Electrodeposited Cu$_2$O Films. J. Phys. Chem. C 2010, 114, 11551−11556.
(5) Chiang, C.-Y.; Aroh, K.; Franson, N.; Satsangi, V. R.; Dass, S.; Ehrman, S. Copper Oxide Nanoparticle Made by Flame Spray Pyrolysis for Photoelectrochemical Water Splitting − Part II. Photoelectrochemical Study. Int. J. Hydrogen Energy 2011, 36, 15519−15526.

(6) Izaki, M.; Nagai, M.; Maeda, K.; Mohamad, F. B.; Motomura, K.; Sasano, J.; Shinagawa, T.; Watase, S. Electrodeposition of 1.4eV Bandgap p-Copper (II) Oxide Film with Excellent Photoactivity. J. Electrochem. Soc. 2011, 158, D578−D584.

(7) Paracchino, A.; Laporte, V.; Sivula, K.; Gra¨tzel, M.; Thimsen, E. Highly Active Oxide Photocathode for Photoelectrochemical Water Reduction. Nat. Mater. 2011, 10, 456−461.

(8) Chiang, C. Y.; Epstein, J.; Brown, A.; Munday, J. N.; Culver, J. N.; Ehrman, S. Biological Templates for Antireflective Current Collectors for Photoelectrochemical Cell Applications. Nano Lett. 2012, 12, 6005−6011.

(9) Chiang, C.-Y.; Chang, M.-H.; Liu, H.-S.; Tai, C. Y.; Ehrman, S. Process Intensification in the Production of Photocatalysts for Solar Hydrogen Generation. Ind. Eng. Chem. Res. 2012, 51, 5207−5215.

(10) Chiang, C.-Y.; Shin, Y.; Aroh, K.; Ehrman, S. Copper Oxide Photocathodes Prepared by A Solution Based Process. Int. J. Hydrogen Energy 2012, 37, 8232−8239.

(11) Paracchino, A.; Mathews, N.; Hisatomi, T.; Stefik, M.; Tilley, S. D.; Gra¨tzel, M. Ultrathin Films on Copper(i) Oxide Water Splitting Photocathodes: A Study on Performance and Stability. Energy Environ. Sci. 2012, 5, 8673−8681.

(12) Parmar, M.; Rajanna, K. Platinum Surface Additive Based Nanostructured CuO Films for Ethanol Sensing. Sensors; IEEE: 2012; pp 1−4.

(13) Zhang, Z.; Wang, P. Highly Stable Copper Oxide Composite as An Effective Photocathode for Water Splitting via A Facile Electrochemical Synthesis Strategy. J. Mater. Chem. 2012, 22, 2456−2464.

(14) Guo, X.; Diao, P.; Xu, D.; Huang, S.; Yang, Y.; Jin, T.; Wu, Q.; Xiang, M.; Zhang, M. CuO/Pd Composite Photocathodes for Photoelectrochemical Hydrogen Evolution Reaction. Int. J. Hydrogen Energy 2014, 39, 7686−7696.

(15) Lim, Y.-F.; Chua, C. S.; Lee, C. J. J.; Chi, D. Sol−Gel Deposited Cu_2O and CuO Thin Films for Photocatalytic Water Splitting. Phys. Chem. Chem. Phys. 2014, 16, 25928−25934.

(16) Morales-Guio, C. G.; Tilley, S. D.; Vrubel, H.; Gratzel, M.; Hu, X. Hydrogen Evolution from A Copper(I) Oxide Photocathode Coated with An Amorphous Molybdenum Sulphide Catalyst. Nat. Commun. 2014, 5, 3059.

(17) Jang, Y. J.; Jang, J.-W.; Choi, S. H.; Kim, J. Y.; Kim, J. H.; Youn, D. H.; Kim, W. Y.; Han, S.; Lee, J. S. Tree Branch-Shaped Cupric Oxide for Highly Effective Photoelectrochemical Water Reduction. Nanoscale 2015, 7, 7624−7631.

(18) Wang, J.; Zhang, W.-D.; Ouyang, W.-X.; Yu, Y.-X. Hierarchically Branched ZnO/CuO Thin Film with Enhanced Visible Light Photoelectrochemical Property. Mater. Lett. 2015, 154, 44−46.

(19) Basnet, P.; Zhao, Y. Tuning the CuxO Nanorod Composition for Efficient Visible Light Induced Photocatalysis. Catal. Sci. Technol. 2016, 6, 2228−2328.

(20) Barreca, D.; Gasparotto, A.; Maccato, C.; Tondello, E.; Lebedev, O. I.; Van Tendeloo, G. CVD of Copper Oxides from a β-diketonate Diamine Precursor: Tailoring the Nano-Organization. Cryst. Growth Des. 2009, 9, 2470−2480.

(21) Artioli, G. A.; Mancini, A.; Barbieri, V. R.; Quattrini, M. C.; Quartarone, E.; Mozzati, M. C.; Drera, G.; Sangaletti, L.; Gombac, V.; Fornasiero, P. Correlation between Deposition Parameters and Hydrogen Production in CuO Nanostructured Thin Films. Langmuir 2016, 32, 1510−1520.

(22) Wang, P.; Ng, Y. H.; Amal, R. Embedment of Anodized p-type Cu_2O Thin Films with CuO Nanowires for Improvement in Photoelectrochemical Stability. Nanoscale 2013, 5, 2952−2958.

(23) Masudy-Panah, S.; Siavash Moakhar, R.; Chua, C. S.; Tan, H. R.; Wong, T. I.; Chi, D.; Dalapati, G. K. Nanocrystal Engineering of Sputter-grown CuO Photocathode for Visible-light-driven Electrochemical Water Splitting. ACS Appl. Mater. Interfaces 2016, 8, 1206−13.

(24) Chen, L.; Shet, S.; Tang, H.; Wang, H.; Deutsch, T.; Yan, Y.; Turner, J.; Al-Jassim, M. Electrochemical Deposition of Copper Oxide Nanowires for Photoelectrochemical Applications. J. Mater. Chem. 2010, 20, 6962−6967.

(25) Lee, S. W.; Lee, Y. S.; Heo, J.; Siah, S. C.; Chua, D.; Brandt, R. E.; Kim, S. B.; Mailoa, J. P.; Buonassisi, T.; Gordon, R. G. Improved Cu_2O-based Solar Cells Using Atomic Layer Deposition to Control the Cu Oxidation State at the p-n Junction. Adv. Energy Mater. 2014, 4, 1301916.

(26) Lee, Y. S.; Chua, D.; Brandt, R. E.; Siah, S. C.; Li, J. V.; Mailoa, J. P.; Lee, S. W.; Gordon, R. G.; Buonassisi, T. Atomic Layer Deposited Gallium Oxide Buffer Layer Enables 1.2 V Open-circuit Voltage in Cuprous Oxide Solar Cells. Adv. Mater. 2014, 26, 4704−4710.

(27) Masudy-Panah, S.; Dalapati, G. K.; Radhakrishnan, K.; Kumar, A.; Tan, H. R. Reduction of Cu-Rich Interfacial Layer and Improvement of Bulk CuO Property Through Two-Step Sputtering for p-CuO/n-Si Heterojunction Solar Cell. J. Appl. Phys. 2014, 116, 074501.

(28) Dalapati, G. K.; Kajen, R. S.; Masudy-Panah, S.; Sonar, P. Defect Analysis of Sputter Grown Cupric Oxide for Optical and Electronics Application. J. Phys. D: Appl. Phys. 2015, 48, 495104.

(29) Masudy-Panah, S.; Radhakrishnan, K.; Tan, H. R.; Yi, R.; Wong, T. I.; Dalapati, G. K. Titanium Doped Cupric Oxide for Photovoltaic Application. Sol. Energy Mater. Sol. Cells 2015, 140, 266−274.

(30) Katayama, J.; Ito, K.; Matsuoka, M.; Tamaki, J. Performance of Cu_2O/ZnO Solar Cell Prepared by Two-step Electrodeposition. J. Appl. Electrochem. 2004, 34, 687−692.

(31) Akimoto, K.; Ishizuka, S.; Yanagita, M.; Nawa, Y.; Paul, G. K.; Sakurai, T. Thin Film Deposition of Cu_2O and Application for Solar Cells. Sol. Energy 2006, 80, 715−722.

(32) Jeong, S.; Mittiga, A.; Salza, E.; Masci, A.; Passerini, S. Electrodeposited ZnO/Cu_2O Heterojunction Solar Cells. Electrochim. Acta 2008, 53, 2226−2231.

(33) Cui, J.; Gibson, U. J. A Simple Two-Step Electrodeposition of Cu_2O/ZnO Nanopillar Solar Cells. J. Phys. Chem. C 2010, 114, 6408−6412.

(34) Rai, P.; Khan, R.; Raj, S.; Majhi, S. M.; Park, K.-K.; Yu, Y.-T.; Lee, I.-H.; Sekhar, P. K. Au@Cu_2O Core−shell Nanoparticles as Chemiresistors for Gas Sensor Applications: Effect of Potential Barrier Modulation on The Sensing Performance. Nanoscale 2014, 6, 581−588.

(35) Azevedo, J.; Steier, L.; Dias, P.; Stefik, M.; Sousa, C.; Araujo, J.; Mendes, A.; Graetzel, M.; Tilley, S. On the Stability Enhancement of Cuprous Oxide Water Splitting Photocathodes by Low Temperature Steam Annealing. Energy Environ. Sci. 2014, 7, 4044−4052.

(36) Zhu, L.; Hong, M.; Ho, G. W. Fabrication of Wheat Grain Textured TiO_2/CuO Composite Nanofibers for Enhanced Solar H_2 Generation and Degradation Performance. Nano Energy 2015, 11, 28−37.

(37) Gao, S.; Sun, Y.; Lei, F.; Liu, J.; Liang, L.; Li, T.; Pan, B.; Zhou, J.; Xie, Y. Freestanding Atomically-thin Cuprous Oxide Sheets for Improved Visible-Light Photoelectrochemical Water Splitting. Nano Energy 2014, 8, 205−213.

(38) Morales, J.; Sanchez, L.; Bijani, S.; Martınez, L.; Gabas, M.; Ramos-Barrado, J. Electrodeposition of Cu_2O: An Excellent Method for Obtaining Films of Controlled Morphology and Good Performance in Li-Ion Batteries. Electrochem. Solid-State Lett. 2005, 8, A159−A162.

(39) Lee, Y.; Leu, I.; Liao, C.; Chang, S.; Wu, M.; Yen, J.; Fung, K. Fabrication and Characterization of Cu_2O Nanorod Arrays and Their Electrochemical Performance in Li-ion Batteries. Electrochem. Solid-State Lett. 2006, 9, A207−A210.

(40) Bijani, S.; Gaba´s, M.; Martínez, L.; Ramos-Barrado, J.; Morales, J.; Sanchez, L. Nanostructured Cu_2O Thin Film Electrodes Prepared by Electrodeposition for Rechargeable Lithium Batteries. Thin Solid Films 2007, 515, 5505−5511.

(41) Schultze, J. W.; Lohrengel, M. Stability, Reactivity and Breakdown of Passive FIlms. Problems of Recent and Future Research. Electrochim. Acta 2000, 45, 2499−2513.

(42) Cheng, S.-L.; Chen, M.-F.; Chung, C.-H. Synthesis and Growth Kinetics of Large-scale CuO Nanowires Grown by Oxidation of Cu Films, Nanoelectronics Conference (INEC), 2011 IEEE 4th International; IEEE: 2011; pp 1−2.

(43) Lee, M.-W.; Park, J.-J.; Kim, D.-Y.; Yoon, S. S.; Kim, H. Y.; Kim, D.; James, S. C.; Chandra, S.; Coyle, T.; Ryu, J. Optimization of Supersonic Nozzle Flow for Titanium Dioxide Thin-film Coating by Aerosol Deposition. J. Aerosol Sci. 2011, 42, 771−780.

(44) Lee, M.-W.; Park, J.-J.; Kim, D.-Y.; Yoon, S. S.; Kim, H.-Y.; James, S. C.; Chandra, S.; Coyle, T. Numerical Studies on the Effects of Stagnation Pressure and Temperature on Supersonic Flow Characteristics in Cold Spray Applications. J. Therm. Spray Technol. 2011, 20, 1085−1097.

(45) Lee, J.-G.; Kim, D.-Y.; Kang, B.; Kim, D.; Song, H.-e.; Kim, J.; Jung, W.; Lee, D.; Al-Deyab, S. S.; James, S. C.; Yoon, S. S. Nickel−copper Hybrid Electrodes Self-adhered onto A Silicon Wafer by Supersonic Cold-spray. Acta Mater. 2015, 93, 156−163.

(46) Lee, J.-G.; Kim, D.-Y.; Mali, M. G.; Al-Deyab, S. S.; Swihart, M. T.; Yoon, S. S. Supersonically Blown Nylon-6 Nanofibers Entangled with Graphene Flakes for Water Purification. Nanoscale 2015, 7, 19027−19035.

(47) Kim, D. Y.; Sinha-Ray, S.; Park, J. J.; Lee, J. G.; Cha, Y. H.; Bae, S. H.; Ahn, J. H.; Jung, Y. C.; Kim, S. M.; Yarin, A. L.; Yoon, S. S. Self-Healing Reduced Graphene Oxide Films by Supersonic Kinetic Spraying. Adv. Funct. Mater. 2014, 24, 4986−4995.

(48) Kim, D. Y.; Park, J. J.; Lee, J. G.; Lee, M. W.; Kim, H. Y.; Oh, J. H.; Seong, T. Y.; Kim, D.; James, S. C.; Hest, M. F.; Chandra, S.; Yoon, S. S. Tuning Hydrophobicity with Honeycomb Surface Structure and Hydrophilicity with CF_4 Plasma Etching for Aerosoldeposited Titania Films. J. Am. Ceram. Soc. 2012, 95, 3955−3961.

(49) Valladares, L. D. L. S.; Salinas, D. H.; Dominguez, A. B.; Najarro, D. A.; Khondaker, S.; Mitrelias, T.; Barnes, C.; Aguiar, J. A.; Majima, Y. Crystallization and Electrical Resistivity of Cu_2O and CuO Obtained by Thermal Oxidation of Cu Thin Films on SiO_2/Si Substrates. Thin Solid Films 2012, 520, 6368−6374.

(50) Xu, J.; Ji, W.; Shen, Z.; Li, W.; Tang, S.; Ye, X.; Jia, D.; Xin, X. Raman Spectra of CuO Nanocrystals. J. Raman Spectrosc. 1999, 30, 413−415.

(51) Fuentes, S.; Zar´ate, R.; Munoz, P.; DIa´z-Droguett, D. E. Formation of Hierarchical CuO Nanowires on A Copper Surface via A Room-Temperature Solution-Immersion Process. J. Chil. Chem. Soc. 2010, 55, 147−149.

(52) Hagemann, H.; Bill, H.; Walker, E.; Franc¸ois, M. Raman Spectra of Single Crystal CuO. Solid State Commun. 1990, 73, 447−451.

(53) Tsai, Y.-H.; Chanda, K.; Chu, Y.-T.; Chiu, C.-Y.; Huang, M. H. Direct Formation of Small Cu_2O Nanocubes, Octahedra, and Octapods for Efficient Synthesis of Triazoles. Nanoscale 2014, 6, 8704−8709.

(54) Zhang, Y. C.; Tang, J. Y.; Wang, G. L.; Zhang, M.; Hu, X. Y. Facile Synthesis of Submicron Cu_2O and CuO Crystallites from A Solid Metallorganic Molecular Precursor. J. Cryst. Growth 2006, 294, 278−282.

(55) Markoulaki, V.; Papadas, I.; Kornarakis, I.; Armatas, G. Synthesis of Ordered Mesoporous CuO/CeO_2 Composite Frameworks as Anode Catalysts for Water Oxidation. Nanomaterials 2015, 5, 1971−1984.

(56) Wang, Y.; Lu¨, Y.; Zhan, W.; Xie, Z.; Kuang, Q.; Zheng, L. Synthesis of Porous Cu_2O/CuO Cages Using Cu-based Metal−organic Frameworks as Templates and Their Gas-sensing Properties. J. Mater. Chem. A 2015, 3, 12796−12803.

(57) Liu, Y.; Gibbs, M.; Puthussery, J.; Gaik, S.; Ihly, R.; Hillhouse, H. W.; Law, M. Dependence of Carrier Mobility on Nanocrystal Size and Ligand Length in PbSe Nanocrystal Solids. Nano Lett. 2010, 10, 1960−1969.

(58) Horowitz, G.; Hajlaoui, M. Grain Size Dependent Mobility in Polycrystalline Organic Field-effect Transistors. Synth. Met. 2001, 122, 185−189.

(59) Hsu, Y.-K.; Yu, C.-H.; Lin, H.-H.; Chen, Y.-C.; Lin, Y.-G. Template Synthesis of Copper Oxide Nanowires for Photoelectrochemical Hydrogen Generation. J. Electroanal. Chem. 2013, 704, 19−23.

(60) Kim, D.-Y.; Joshi, B. N.; Lee, J.-G.; Lee, J.-H.; Lee, J. S.; Hwang, Y. K.; Chang, J.-S.; Al-Deyab, S.; Tan, J.-C.; Yoon, S. S. Supersonic Cold Spraying for Zeolitic Metal−organic Framework Films. Chem. Eng. J. 2016, 295, 49−56.

(61) Saito, R.; Miseki, Y.; Sayama, K. Highly Efficient Photoelectrochemical Water Splitting Using A Thin Film Photoanode of $BiVO_4/SnO_2/WO_3$ Multi-composite in A Carbonate Electrolyte. Chem. Commun. 2012, 48, 3833−3835.